


 Cite this: *Chem. Commun.*, 2022, 58, 13019

 Received 12th August 2022,  
 Accepted 28th October 2022

DOI: 10.1039/d2cc04497h

rsc.li/chemcomm

# Dynamics of the alkyne → copper(i) interaction and its use in a heteroleptic four-component catalytic rotor†

 Suchismita Saha,<sup>a</sup> Sohom Kundu,<sup>a</sup> Pronay Kumar Biswas,<sup>a</sup> Michael Bolte<sup>id</sup> <sup>b</sup> and Michael Schmittel<sup>id</sup> \*<sup>a</sup>

The HETPYNE (HETeroleptic Phenanthroline and alkyNE metal) and DABCO-(zinc porphyrin)<sub>2</sub> interactions were used to assemble the four-component nanorotor ROT-1 that exhibited a highly dynamic alkyne → copper(i) dissociation ( $k_{298} = 240$  kHz) at 298 K. Quantitative click reaction transformed ROT-1 into the new rotor ROT-2 ( $k_{298} = 77$  kHz) with a triazole → copper(i) linkage thus opening perspectives for bioorthogonal click strategies to biohybrid machinery.

Inspired by nanomechanical motions<sup>1</sup> in biological machines,<sup>2–4</sup> scientists have developed an enormous interest in the development of artificial molecular devices.<sup>5–8</sup> Among them, molecular motors,<sup>9–11</sup> rotors,<sup>12</sup> shuttles,<sup>13–15</sup> tweezers,<sup>16–18</sup> turnstiles,<sup>19</sup> muscles,<sup>20</sup> elevators,<sup>21</sup> pumps,<sup>10</sup> walkers<sup>22</sup> etc.<sup>5–8</sup> are well studied. Though numerous examples of artificial covalent molecular devices are known in the literature,<sup>5–8</sup> evolution toward multi-component artificial machineries still represents a major challenge due to the limited amount of dynamic orthogonality in hetero-assemblies.<sup>23,24</sup>

For designing artificial multicomponent rotors, orthogonal dynamic interactions are a key requirement.<sup>25</sup> To the best of our knowledge, all literature known dynamic interactions that have been used to construct artificial multicomponent rotors are derived from H-bonding or *N,O*-donor<sup>19</sup> metal interactions.<sup>26–30</sup> Clearly, development of any new dynamic interaction will open further opportunities. Here, we demonstrate for the first time a supramolecular assembly and a rotor built on the dynamic alkyne → copper(i) interaction.<sup>31,32</sup> Specifically, we designed a four-component supramolecular assembly and nanorotor based



Fig. 1 (a) Chemical structure and cartoon representation of the ligands **1**, **2**, **3** and DABCO. (b) Cartoon representation of the four-component assembly **ASB-1** and nanorotor **ROT-1**.

on the heteroleptic Cu<sup>+</sup>-phenanthroline alkyne (HETPYNE: HETeroleptic Phenanthroline and alkyNE metal) complexation (Fig. 1). Addition of stoichiometric quantities of azide to the rotor afforded the new class of a Cu<sup>+</sup>-triazole rotor through an *in situ* copper(i) catalysed click reaction.

For our study, we decided to use the phenanthroline-appended zinc(ii) porphyrin ligands **1** or **2** as stator. Bulky aryl groups<sup>33</sup> at the 2,9-position of the phenanthroline phenAr<sub>2</sub> are essential to avoid the unwanted formation of the corresponding homoleptic Cu<sup>+</sup> complexes.<sup>34–36</sup> In order to design rotator **3**, we performed a few model experiments to evaluate the binding of a terminal ethynyl group to [Cu(phenAr<sub>2</sub>)]<sup>+</sup>. Mixing of **4**, **5** and [Cu(CH<sub>3</sub>CN)<sub>4</sub>]PF<sub>6</sub> in 1:1:1 ratio (2.5 mM each) in CD<sub>2</sub>Cl<sub>2</sub> accomplished quantitative formation of **C1** = [Cu(**4**)(**5**)]<sup>+</sup> (Fig. 2a). In the <sup>1</sup>H NMR, a downfield shift of all phenanthroline protons indicated binding of **5** to [Cu(**4**)]<sup>+</sup>, for instance, proton 4''-H shifted from 8.67 to 8.74 ppm and 5''-H from

<sup>a</sup> Center of Micro and Nanochemistry and (Bio)Technology, Organische Chemie I, Universität Siegen, Adolf-Reichwein-Str. 2, Siegen D-57068, Germany. E-mail: schmittel@chemie.uni-siegen.de; Tel: +49(0) 2717404356

<sup>b</sup> Institut für Organische Chemie und Chemische Biologie, Johann Wolfgang Goethe-Universität, Max-von-Laue Strasse 7, Frankfurt am Main D-60438, Germany

† Electronic supplementary information (ESI) available: Experimental procedures, compound characterizations, spectral data, NMR titration, and VT-<sup>1</sup>H-NMR kinetics. CCDC 2199510. For ESI and crystallographic data in CIF or other electronic format see DOI: <https://doi.org/10.1039/d2cc04497h>





**Fig. 2** (a) Formation of model complex **C1**. (b) Partial  $^1\text{H}$  NMR (400 MHz, 298 K) of  $[\text{Cu}(\mathbf{4})]^+$ , **5** and **C1** in  $\text{CD}_2\text{Cl}_2$  (2.5 mM). (c) X-ray crystal structure of complex **C1**. Carbons are shown in light grey; H, light green; N, blue; O, red;  $\text{Cu}^+$ , cyan and I, violet.

8.14 to 8.20 ppm (Fig. 2b). In contrast, protons d'-H (from 6.77 to 6.60 ppm) and e'-H (from 4.68 to 4.09 ppm) of the ethynyl ligand **5** shifted upfield upon its complexation to  $[\text{Cu}(\mathbf{4})]^+$ , due to the shielding of these protons by the  $\pi$ -ring current of the mesityl groups. On the other hand, despite being in the shielding region of a strong  $\pi$ -electron cloud, the downfield shift of proton f'-H (from 5 to **C1**: 2.58 to 2.68 ppm) validated the ethynyl binding to the  $\text{Cu}^+$  center. Single crystal X-ray analysis of **C1** revealed a triclinic crystal system with the space group  $P\bar{1}$  (ESI,† Fig. S27). Importantly, it clearly demonstrated the side-on binding of  $\text{Cu}^+$  to both ethynyl carbons whereas there was no binding visible between oxygen and  $\text{Cu}^+$  center (Fig. 2c). The solid state structure disclosed the bond lengths of Cu(1)–C(41), Cu(1)–C(42), Cu(1)–N(11) and Cu(1)–N(1) to be 1.958(5) Å, 1.969(4) Å, 2.002(3) Å and 2.013(3) Å, respectively. The angle between the planes defined by N(1)–Cu(1)–N(11) and C(41)–Cu(1)–C(42) was determined as  $16^\circ$ . This geometry around the copper(i) center is not very common. From an NMR titration, the binding constant of **5** to  $[\text{Cu}(\mathbf{4})]^+$  was determined as  $\log K = 2.81 \pm 0.16$  (ESI,† Fig. S26). We propose to denote the heteroleptic complexation motif between a  $[\text{Cu}(\text{phenAr}_2)]^+$  and an alkyne as HETPYNE interaction (*vide supra*).

After establishing the HETPYNE motif, the zinc(II) porphyrin **3** with two ethynyl terminals was designed. To synthesize ligand **3**, we first reacted 5,15-di(4-iodophenyl)-10,20-dimesityl zinc(II) porphyrin and 4-ethynylphenol under Sonogashira coupling conditions providing the corresponding diphenol. In the final step, a Williamson ether synthesis between the phenol-substituted zinc(II) porphyrin and propargyl bromide in presence of base furnished ligand **3** in 85% yield. Protons e-H of **3** appear in the  $^1\text{H}$  NMR well separated from other proton signals and should serve as good indicator of any binding.

As expected from the model studies, the four-component self-assembly **ASB-1** was quantitatively afforded by mixing DABCO, ligands **1** & **3**, and  $[\text{Cu}(\text{CH}_3\text{CN})_4]\text{PF}_6$  in a 1:1:1:2 ratio in  $\text{CD}_2\text{Cl}_2$  (Fig. 3a). Two characteristic multiplets for the  $\text{CH}_2$ -units of DABCO in the negative region of the  $^1\text{H}$  NMR indicated quantitative formation of the hetero-sandwich complex (Fig. 3b).<sup>37</sup> Significant changes at all phenanthroline protons in the  $^1\text{H}$  NMR upon moving from  $[\text{Cu}_2(\mathbf{1})]^{2+}$  to **ASB-1** supported the binding of **3** to the copper(i)-loaded phenanthroline stations (Fig. 3c and d).



**Fig. 3** (a) Cartoon representation of the four-component self-assembly leading to the formation of **ASB-1**. (b) DABCO-H signal of **ASB-1** in  $^1\text{H}$  NMR ( $\text{CD}_2\text{Cl}_2$ , 400 MHz, 298 K). Partial  $^1\text{H}$  NMR ( $\text{CD}_2\text{Cl}_2$ , 400 MHz, 298 K) of **1**,  $[\text{Cu}_2(\mathbf{1})]^{2+}$ , **3** and **ASB-1** showing the (c) aromatic and (d) aliphatic region.

Downfield shift of proton f-H from 2.64 to 3.10 ppm in **ASB-1** attested the terminal ethynyl binding of **3** at the  $\text{Cu}^+$  center of **1** (Fig. 3d). Drastic upfield shifts of proton signal e-H from 4.79 to 3.60 ppm and of d-H from 7.05 to 6.77 ppm along with a downfield shift of proton signal c-H from 7.64 to 7.75 ppm validated the formation of the HETPYNE complex. Furthermore, a single peak in the ESI-MS at  $m/z = 1489.1$  confirmed formation of the hetero-assembly (ESI,† Fig. S23) and a single diffusion trace in the  $^1\text{H}$ -DOSY NMR representing structure **ASB-1** excluded the presence of other undesired assemblies (ESI,† Fig. S20).

The clean formation of the heteroleptic sandwich complex encouraged us to test the HETPYNE motif as a dynamic interaction in a multicomponent rotor. To assemble the rotor, we selected zinc(II) porphyrin **2** containing just one phenanthroline station as stator and ligand **3** as rotator. Dissolving the ligands **2**, **3**, DABCO and  $[\text{Cu}(\text{CH}_3\text{CN})_4]\text{PF}_6$  in a 1:1:1:1 ratio in  $\text{CD}_2\text{Cl}_2$  quantitatively furnished rotor **ROT-1** irrespective of the sequence of addition (Fig. 4a). As in **ASB-1**, two broad signals in the negative region corresponding to DABCO and significant shifts of all phenanthroline protons in the  $^1\text{H}$  NMR validated formation of the heteroassembly (Fig. 4b–d). Upfield shifts of rotor proton signals e-H from 4.79 to 4.19 ppm along with downfield shift of f-H from 2.64 to 2.88 ppm authenticated the rotor structure (Fig. 4c and d). Its formation was further confirmed by DOSY NMR and ESI-MS data (ESI,† Fig. S21 and S24).

A single set of  $^1\text{H}$  NMR signals for protons c-H, d-H, e-H and f-H of **ROT-1** suggested fast rotation of the rotor on the NMR



**Fig. 4** (a) Cartoon representation of the self-assembly of rotor **ROT-1** from four components. (b)  $(\text{CH}_2)_{\text{DABCO}}$  signal of **ROT-1** in the  $^1\text{H}$  NMR ( $\text{CD}_2\text{Cl}_2$ , 400 MHz). Partial  $^1\text{H}$  NMR ( $\text{CD}_2\text{Cl}_2$ , 400 MHz, 298 K) of **2**,  $[\text{Cu}(\mathbf{2})]^+$ , **3** and **ROT-1** in the (c) aromatic and (d) aliphatic region.



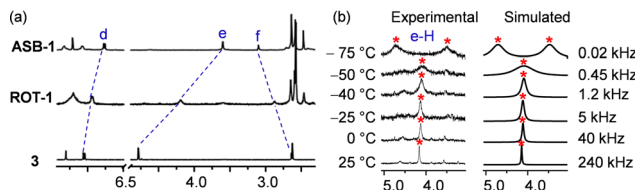


Fig. 5 (a) Partial  $^1\text{H}$  NMR ( $\text{CD}_2\text{Cl}_2$ , 400 MHz, 298 K) of **3**, **ROT-1** and **ASB-1**. (b) VT- $^1\text{H}$  NMR ( $\text{CD}_2\text{Cl}_2$ , 600 MHz) of **ROT-1** exhibiting the splitting of proton signal e-H into a 1:1 set and the corresponding rotational frequency at different temperatures.

time scale (Fig. 4c and d). Comparison of the  $^1\text{H}$  NMR spectra of the free rotator **3**, **ROT-1** and **ASB-1** showed that the proton signals d-H, e-H and f-H of rotor **ROT-1** appeared approximately in the averaged position of those of free **3** and **ASB-1** (Fig. 5a). Variable temperature (VT)  $^1\text{H}$  NMR of **ROT-1** was thus performed to evaluate its dynamic behavior. Upon lowering the temperature, the sharp singlet at 4.19 ppm corresponding to proton e-H broadened and split into two singlets in a 1:1 ratio at  $-75\text{ }^\circ\text{C}$  with a coalescence temperature around  $-50\text{ }^\circ\text{C}$  (Fig. 5b). The upfield signal at 3.50 ppm was assigned to the HETPYNE-complexed proton e-H and the downfield signal at 4.71 ppm is ascribed to proton e-H at the uncomplexed arm. The rotational frequency of the rotor at different temperatures was evaluated using winDNMR-based spectral simulations.<sup>38</sup> The activation data for the rotation was derived from the Eyring plot (Table 1 and ESI,† Fig. S18). The rotational frequency turned out to be 240 kHz at  $25\text{ }^\circ\text{C}$  and  $\Delta G_{298}^\ddagger = 42.5\text{ kJ mol}^{-1}$ .

After the clean formation of rotor **ROT-1**, our next target was the *in situ* rotor-to-rotor transformation. The presence of a copper(i) ion and terminal alkynes in the rotor suggested a conversion of **ROT-1** to a triazole rotor through an *in situ* click reaction. For this purpose, 2.0 equiv. of benzyl azide was added to **ROT-1** in  $\text{CD}_2\text{Cl}_2$  (Fig. 6a). To accelerate the reaction, 1  $\mu\text{L}$  of  $\text{Et}_3\text{N}$  was added. After 24 h of heating at  $40\text{ }^\circ\text{C}$ , the solvent was evaporated to remove  $\text{NEt}_3$  and the residue was redissolved in  $\text{CD}_2\text{Cl}_2$ .  $^1\text{H}$  NMR showed quantitative formation of **ROT-2** and a disappearance of the proton signal f-H (Fig. 6b). Upon moving from **ROT-1** to **ROT-2**, characteristic shifts for all phenanthroline protons were observed. The downfield shift of proton signal e-H (from 4.19 to 4.81 ppm), upfield shifts of proton signals d-H (from 6.93 to 6.78 ppm) and c-H (from 7.72 ppm to 7.61 ppm) along with the appearance of a new singlet at 5.52 ppm (j-H) corroborated the formation of **ROT-2**. The broad signal of the DABCO protons at  $-4.39$  ppm confirmed the

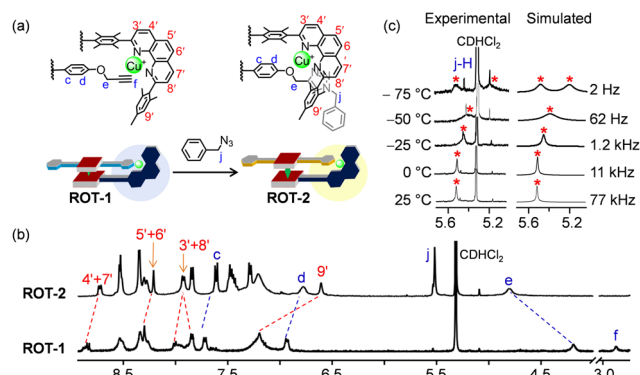


Fig. 6 (a) *In situ* transformation of **ROT-1** to **ROT-2** upon addition of 2.0 equiv. of benzyl azide. (b) Partial  $^1\text{H}$  NMR ( $\text{CD}_2\text{Cl}_2$ , 400 MHz, 298 K) of **ROT-1** and **ROT-2**. (c) VT- $^1\text{H}$  NMR ( $\text{CD}_2\text{Cl}_2$ , 600 MHz) of **ROT-2** showing splitting of the proton signal j-H (1:1 ratio) and the corresponding rotational frequency at different temperatures.

intactness of the assembly (ESI,† Fig. S15). **ROT-2** was further characterized by ESI-MS and DOSY NMR data (ESI,† Fig. S25 and S22).

A single set of  $^1\text{H}$  NMR signals for protons c-H, d-H, e-H and j-H of **ROT-2** indicated a fast rotation on the NMR time scale. Upon performing the VT  $^1\text{H}$  NMR the proton signal for j-H split into two singlets in 1:1 ratio at  $-75\text{ }^\circ\text{C}$  (Fig. 6c). Rotational frequencies at different temperature along with activation parameters were calculated (Fig. 6c and Table 1). The facile transformation of the self-catalyzing rotor **ROT-1** to rotor **ROT-2** opens interesting perspectives to generate biohybrid materials *via* bioorthogonal click reactions.<sup>39</sup>

In conclusion, we have synthesized a four-component hetero-sandwich complex and a four-component rotor based on the dynamic  $[\text{Cu}(\text{phenAr}_2)(\text{alkyne})]^+$  motif. Though alkyne  $\rightarrow$  copper(i) interactions are well known in the literature,<sup>40</sup> for the first time its high dynamics has been determined and used to assemble a high-speed multicomponent rotor. The utility of this dynamic orthogonal motif in supramolecular rotors opens new venues for molecular machines. Furthermore, a successful quantitative transformation of the  $\text{Cu}^+$ -alkyne rotor to a new  $\text{Cu}^+$ -triazole rotor was achieved through *in situ* click reaction. It is expected that thermal self-catalyzing rotors will find their way into diverse applications, *e.g.*, in catalysis,<sup>35,41</sup> biohybrid materials *via* bioorthogonal functionalization<sup>42</sup> and elsewhere.<sup>43</sup>

We are indebted to the Deutsche Forschungsgemeinschaft for continued support under Schm 647/22-1 (No 491092614). We thank Dr Paululat for measuring the VT- $^1\text{H}$  NMR.

Table 1 Exchange frequencies of **ROT-1** and **ROT-2** along with their activation parameters<sup>a</sup>

Rotor	$k_{298}/\text{kHz}$	$\Delta H^\ddagger/\text{kJ mol}^{-1}$	$\Delta S^\ddagger/\text{J K}^{-1} \text{mol}^{-1}$	$\Delta G_{298}^\ddagger/\text{kJ mol}^{-1}$
<b>ROT-1</b>	240	$44.0 \pm 0.2$	$5.0 \pm 0.7$	42.5
<b>ROT-2</b>	77	$50.1 \pm 0.4$	$16.7 \pm 0.6$	45.2

<sup>a</sup> The higher  $\Delta H^\ddagger$  for **ROT-2** than **ROT-1** reflects the stronger binding constant of a triazole to  $[\text{Cu}(4)]^+$  (see triazole **6** in ESI, Fig. S27). As often seen in enthalpy-entropy compensation, strong binding leads to higher positive activation entropy.

## Conflicts of interest

There are no conflicts to declare.

## Notes and references

- M. Dutta and B. Jana, *Chem. Commun.*, 2021, 57, 272–283.
- J. E. Walker, *Biochem. Soc. Trans.*, 2013, 41, 1–16.
- R. D. Vale and R. A. Milligan, *Science*, 2000, 288, 88–95.



- 4 H. Noji, R. Yasuda, M. Yoshida and K. Kinoshita, Jr, *Nature*, 1997, **386**, 299–302.
- 5 A. Goswami, S. Saha, P. Biswas and M. Schmittel, *Chem. Rev.*, 2020, **120**, 125–199.
- 6 S. Kassem, T. van Leeuwen, A. S. Lubbe, M. R. Wilson, B. L. Feringa and D. A. Leigh, *Chem. Soc. Rev.*, 2017, **46**, 2592–2621.
- 7 S. Erbas-Cakmak, D. A. Leigh, C. T. McTernan and A. L. Nussbaumer, *Chem. Rev.*, 2015, **115**, 10081–10206.
- 8 A. J. McConnell, C. S. Wood, P. P. Neelakandan and J. R. Nitschke, *Chem. Rev.*, 2015, **115**, 7729–7793.
- 9 S. Kassem, T. van Leeuwen, A. S. Lubbe, M. R. Wilson, B. L. Feringa and D. A. Leigh, *Chem. Soc. Rev.*, 2017, **46**, 2592–2621.
- 10 Y. Feng, M. Ovalle, J. S. W. Seale, C. K. Lee, D. J. Kim, R. D. Astumian and J. F. Stoddart, *J. Am. Chem. Soc.*, 2021, **143**, 5569–5591.
- 11 M. Baroncini, S. Silvi and A. Credi, *Chem. Rev.*, 2020, **120**, 200–268.
- 12 B. Lin, I. Karki, P. J. Pellechia and K. D. Shimizu, *Chem. Commun.*, 2022, **58**, 5869–5872.
- 13 T. Kumpulainen, M. R. Panman, B. H. Bakker, M. Hilbers, S. Woutersen and A. M. Brouwer, *J. Am. Chem. Soc.*, 2019, **141**, 19118–19129.
- 14 H. V. Schröder, F. Stein, J. M. Wollschläger, S. Sobottka, M. Gaedke, B. Sarkar and C. A. Schalley, *Angew. Chem., Int. Ed.*, 2019, **58**, 3496–3500.
- 15 J. E. M. Lewis, R. J. Bordoli, M. Denis, C. J. Fletcher, M. Galli, E. A. Neal, E. M. Rochette and S. M. Goldup, *Chem. Sci.*, 2016, **7**, 3154–3161.
- 16 B. Doistau, L. Benda, J.-L. Cantin, L.-M. Chamoreau, E. Ruiz, V. Marvaud, B. Hasenknopf and G. Vives, *J. Am. Chem. Soc.*, 2017, **139**, 9213–9220.
- 17 H. Yoon, J. M. Lim, H.-C. Gee, C.-H. Lee, Y.-H. Jeong, D. Kim and W.-D. Jang, *J. Am. Chem. Soc.*, 2014, **136**, 1672–1679.
- 18 A. Petitjean, R. G. Khoury, N. Kyritsakas and J.-M. Lehn, *J. Am. Chem. Soc.*, 2004, **126**, 6637–6647.
- 19 B. Godde, A. Jouaiti, A. Fluck, N. Kyritsakas, M. Mauro and M. W. Hosseini, *Dalton Trans.*, 2017, **46**, 14897–14906.
- 20 M. C. Jimenez, C. O. Dietrich-Buchecker and J.-P. Sauvage, *Angew. Chem., Int. Ed.*, 2000, **39**, 3284–3287.
- 21 J. D. Badjic, V. Balzani, A. Credi, S. Silvi and J. F. Stoddart, *Science*, 2004, **303**, 1845–1849.
- 22 M. von Delius, E. M. Geertsema and D. A. Leigh, *Nat. Chem.*, 2010, **2**, 96–101.
- 23 M. Schmittel, *Chem. Commun.*, 2015, **51**, 14956–14968.
- 24 M. Schmittel, *Isr. J. Chem.*, 2018, **59**, 197–208.
- 25 P. K. Biswas, S. Saha, Y. Nanaji, A. Rana and M. Schmittel, *Inorg. Chem.*, 2017, **56**, 6662–6670.
- 26 B. E. Dial, P. J. Pellechia, M. D. Smith and K. D. Shimizu, *J. Am. Chem. Soc.*, 2012, **134**, 3675–3678.
- 27 S. Saha, P. K. Biswas and M. Schmittel, *Inorg. Chem.*, 2019, **58**, 3466–3472.
- 28 P. K. Biswas, A. Goswami, S. Saha and M. Schmittel, *Chem. – Eur. J.*, 2020, **26**, 14095–14099.
- 29 I. Paul, A. Goswami, N. Mittal and M. Schmittel, *Angew. Chem., Int. Ed.*, 2018, **57**, 354–358.
- 30 S. Hiraoka, M. Shiro and M. Shionoya, *J. Am. Chem. Soc.*, 2004, **126**, 1214–1218.
- 31 D. Parasar, T. T. Ponduru, A. Noonikara-Poyil, N. B. Jayaratna and H. V. R. Dias, *Dalton Trans.*, 2019, **48**, 15782–15794.
- 32 H. V. R. Dias, J. A. Flores, J. Wu and P. Kroll, *J. Am. Chem. Soc.*, 2009, **131**, 11249–11255.
- 33 S. K. Samanta and M. Schmittel, *J. Am. Chem. Soc.*, 2013, **135**, 18794–18797.
- 34 B. Ralahy, U. Hahn, E. Wasielewski and J.-F. Nierengarten, *Eur. J. Inorg. Chem.*, 2021, 2625–2635.
- 35 S. Saha, A. Ghosh, T. Paululat and M. Schmittel, *Dalton Trans.*, 2020, **49**, 8693–8700.
- 36 S. De, S. Pramanik and M. Schmittel, *Angew. Chem., Int. Ed.*, 2014, **53**, 14255–14259.
- 37 S. K. Samanta, D. Samanta, J. W. Bats and M. Schmittel, *J. Org. Chem.*, 2011, **76**, 7466–7473.
- 38 H. J. Reich, *NMR Spectrum Calculations: WinDNMR, Version 7.1.13*, Department of Chemistry, University of Wisconsin, 2008.
- 39 C. G. Parker and M. R. Pratt, *Cell*, 2020, **180**, 605–632.
- 40 M. Meldal and C. W. Tornøe, *Chem. Rev.*, 2008, **108**, 2952–3015.
- 41 A. Goswami, T. Paululat and M. Schmittel, *J. Am. Chem. Soc.*, 2019, **141**, 15656–15663.
- 42 <https://www.nobelprize.org/uploads/2022/10/popular-chemistryprize2022.pdf>.
- 43 K. T. Fam, L. Saladin, A. S. Klymchenko and M. Collot, *Chem. Commun.*, 2021, **57**, 4807–4810.

